System Identification for Dynamic Modeling of a Bumper Car *

Tobias Petri* Simone Baratto** Giancarlo Ferrari Trecate**

* RWTH Aachen University, Aachen, Germany (e-mail: tobias.petri@rwth-aachen.de)

** École Polytechnique Fédérale de Lausanne, DECODE lab, Lausanne, Switzerland (e-mail:{simone.baratto, giancarlo.ferraritrecate}@epfl.ch)

Abstract: This paper presents the modeling of autonomous vehicles with high maneuverability used in an experimental framework for educational purposes. Since standard bicycle models typically neglect wide steering angles, we develop modified planar bicycle models and combine them with both parametric and non-parametric identification techniques that progressively incorporate physical knowledge. The resulting models are systematically compared to evaluate the tradeoff between model accuracy and computational requirements, showing that physics-informed neural network models surpass the purely physical baseline in accuracy at lower computational cost.

Keywords: Automotive system identification and modeling, Physics informed and grey box model identification, Nonlinear system identification, Machine and deep learning for system identification, Vehicle dynamic systems, Autonomous vehicles

1. INTRODUCTION

Autonomous driving has emerged as a transformative technology, attracting significant attention due to its potential to enhance road safety. Despite consistent progress and strong evidence supporting its safety, public acceptance of autonomous driving remains limited. For instance, the comparative study by Lillo et al. (2023) demonstrated that Waymo's autonomous service achieved markedly fewer injury and property damage claims per mile than human drivers, highlighting its superior safety performance. Nevertheless, societal concerns and limited exposure continue to hinder trust in this technology. Motivated by these observations, we aim at building an experimental platform where autonomous driving safety can be intuitively and convincingly demonstrated. We develop an autonomous bumper car platform that showcases collision avoidance in a playful and interactive manner. Within this setup, visitors can directly engage with the system, attempting to provoke collisions while the vehicle autonomously reacts to prevent them.

In contrast to conventional on-road scenarios, bumper car arenas present unique challenges for planning-based collision avoidance algorithms like Model Predictive Control (MPC), which require sophisticated and accurate vehicle models. Bumper cars possess exceptionally high maneuverability owing to unusually large steering angles (up to approximately 115°). This distinctive feature amplifies nonlinear dynamic effects and invalidates many typical small-angle assumptions that underpin standard vehicle

models, thus motivating careful system identification and model development specific to this experimental domain.

A natural starting point is the family of planar bicycle models, which balance modeling fidelity and computational cost for path-planning and prediction tasks (Jazar, 2008). Two variants are very popular in the literature: the dynamic bicycle model, which is derived from the Newton–Euler formalism and explicitly accounts for tire-force interactions, and the kinematic bicycle model, which is based on the geometric configuration of the vehicle chassis.

The potential application of the bumper car model in planning-based collision avoidance or as a digital twin in testing entails various and sometimes contradictory requirements: While accuracy and computational feasibility are central demands on the bumper car model, generalization and adaptability potentially gain importance in applications where the system is influenced by cyclically changing passengers. For this reason, we seek to explore data-driven modeling approaches that offer the potential for improved adaptability and generalization while maintaining computational efficiency and accuracy.

1.1 Related Work

By considering vehicles dynamics modeling, recent work extends beyond purely first-principles modeling by incorporating data-driven identification within white/grey/black-box pipelines. A typical field of application of such dedicated data-driven models is autonomous racing, where the main control challenge arises from pushing the vehicle to the handling limits. In the following paragraphs, we review relevant works that embody and advance these methodologies.

^{*} This work was supported as a part of NCCR Automation, a National Centre of Competence in Research, funded by the Swiss National Science Foundation (grant number 51NF40_225155).

While Newton-Euler models are close to physical principles, the underlying tire model brings its highest uncertainty. Thus, the parameters of the Magic Formula in Pacejka (2005) are estimated online using a Long Short-Term Memory (LSTM) model in Kim et al. (2022) and Chrosniak et al. (2024). In Paparazzo et al. (2025) the Newton-Euler parameters are updated online using constrained Sparse Identification of Nonlinear Dynamics (SINDy) on recent data, allowing the autonomous system to improve trajectory tracking in an MPC-framework. A linearization of the Newton-Euler model is combined with a Recurrent Neural Network (RNN) residual model in Chen et al. (2024), compensating for nonlinear lateral dynamics.

Another research direction augments the kinematic bicycle model with data-driven residual models to improve predictive accuracy. Using Gaussian Process Regression (GPR) in Jain et al. (2020) and RNNs in Rhode et al. (2024) the authors achieve high-accuracy path tracking in MPC frameworks. The latter work incorporates physical information by modeling either the global motion or only the kinematic state with a neural network, showing that embedding physical laws improves accuracy while reducing network size. Ghosn et al. (2024) proposes an extended kinematic bicycle model in which vehicle velocities are derived under inclusion of tire slip predicted by an LSTM network.

Previous works rely on assumptions that are not always met by high-maneuverable vehicles. First, their reported accuracy can degrade in regimes with advanced steering range and pronounced slip, as encountered on our platform. Second, while Newton-Euler formulations can represent these regimes, their numerical stiffness and integration cost can be prohibitive in real-time applications. To the best of our knowledge, none of the existing models retains the accuracy of high steering Newton-Euler dynamics while achieving kinematic-like computational speed suitable for embedded deployment.

1.2 Contributions

This paper addresses the above research gaps with the following contributions on system identification:

- 1) We tailor a Newton–Euler bicycle model to the bumpercar geometry, actuation, and large steering range, including discretization choices that enable stable multi-step prediction under low-speed. For lateral tire force we propose a partly linear function as a tradeoff between simplicity and accuracy.
- 2) We adapt the extended kinematic formulation of Ghosn et al. (2024) to bumper cars with extended steering, closely tying the system state to the system actuation. On top of the kinematic backbone, we employ the Sparse Identification of Nonlinear Dynamical Systems (SINDy) framework to capture the vehicle state evolution in a physics-consistent manner and Multilayer Perceptron (MLP) neural networks to model the remaining dynamics. Furthermore, through a progressive transition from black-box to grey-box representations, we examine the advantages of embedding physical structure into the learned model.

Based of experimental data we validate the vehicle model accuracy and compare the prediction runtime of the derived models. Additionally, we compare model interpretability and its implications for physically consistent model adaption. The results highlight that kinematic grey-box models approach or surpass the accuracy of the Newton-Euler baseline at substantially lower runtime, making them attractive for real-time use on bumper car.

The remainder of this article is organized as follows. Section 2 introduces the modeling framework and details the adaptation of two conventional vehicle models to the dynamics of a bumper car. In Section 3, data-driven system identification is conducted based on the previously derived models. Section 4 presents the experimental data acquisition and validation. Finally, Section 5 summarizes the main findings and outlines potential directions for future research.

2. BUMPER CAR MODELS

The bumper car is modeled as a rigid body on a plane surface, with its pose $\boldsymbol{p}_k = \left[p_{\mathbf{x}} \ p_{\mathbf{y}} \ \theta\right]_k^T$ defined by the two-dimensional position and the yaw angle. The vehicle motion $\boldsymbol{v}_k = \left[v_{\mathbf{x}} \ v_{\mathbf{y}} \ \omega\right]_k^T$ is defined in body frame by the longitudinal and lateral velocity and the yaw rotation, all referring to the center of gravity (CoG) of the vehicle. The input provided by the driver is $\boldsymbol{u}_k = \left[u_s \ u_m\right]_k^T$.

The bumper car consists a vehicle body with one front wheel and two rear wheels. The front wheel is both steered and motorized, while the rear axle comprises two non-driven wheels. Each component of the bumper car, as depicted in Figure 1, is briefly discussed.

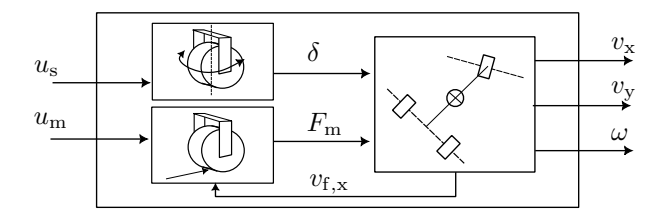


Fig. 1. Block diagram of the bumper car including steering, motor, and vehicle body dynamics.

The stepper motor sets the steering angle δ according to the steering input $u_s \in [-\hat{\delta}, \hat{\delta}]$ with steering range $\hat{\delta} > 0$. The steering angle dynamic is provided by a custom-made embedded controller described by the first-order model

$$\dot{\delta} = \begin{cases} (u_s - \delta)/T_s & \text{for } |u_s - \delta|/T_s < d, \\ \text{sign}(u_s - \delta)d & \text{for } |u_s - \delta|/T_s \ge d \end{cases}$$
 (1)

with maximum steer rate d > 0 and time constant $T_s > 0$.

The motor controller operates in throttle or braking mode depending on the sign of the motor input $u_{\rm m} \in [-1,c]$. A positive input corresponds to a reference velocity limited by c>0, entering a proportional controller that sets the motor force $F_{\rm m}=K_{\rm t}(u_{\rm m}-v_{\rm f,x})$, where $v_{\rm f,x}\in\mathbb{R}$ is the longitudinal front wheel velocity. Negative inputs activate braking mode, modeled as a resistive drag force $F_{\rm m}=u_{\rm m}K_{\rm b}v_{\rm f,x}$.

To model the dynamics of the bumper car, two widely used formulations of the bicycle model are considered in this work: (i) Newton–Euler bicycle models (often simply called dynamic bicycle model (Jazar, 2008)), which consider force-based interactions (tire slip, inertial coupling) and can achieve high fidelity, though requiring more detailed parameterization and greater computational effort; (ii) Kinematic bicycle models, which neglect tire dynamics and exploit geometric constraints for simplicity and fast computation time (Kong et al., 2015).

Under the assumption of small steering angles, small slip angles, and approximately constant longitudinal velocities, the Newton-Euler becomes linear (Jazar, 2008). The linear Newton-Euler model can model moderate tire slip, with moderate complexity in parametrization and evaluation. The linearization assumptions ultimately result in the diminished prediction accuracy illustrated in Figure 2.

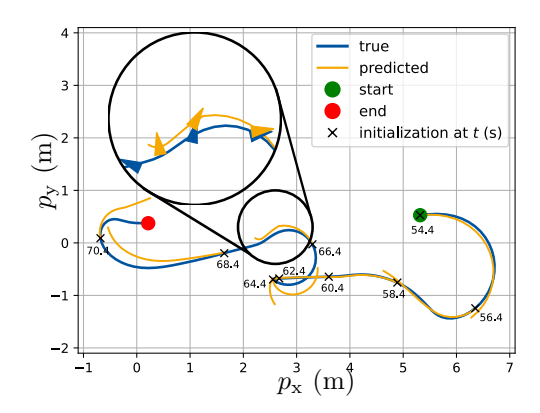


Fig. 2. Comparison between the experimental vehicle trajectory and the predicted trajectory obtained with the linearized Newton-Euler model. The model is reinitialized every two seconds to test its effectiveness in different scenarios. The smaller and bigger circles isolate a specific part of the trajectories and their zoomed-out version, respectively.

The trajectory in the figure illustrates the increased maneuverability of the bumper car due to high steering angles. Between 64.4s and 66.4s the steering angle exceeds 90° and the vehicle transitions between backward and forward motion, as highlighted by the orientation arrows in the zoomed-out trajectories. In these conditions the model fails to accurately predict the actual trajectory. Further limitations result from neglecting deceleration due to tire sliding as seen between 58.4s and 64.4s. These shortcomings clearly underscore the necessity for vehicle models that are reliable across a wide range of operating conditions, while preserving computational feasibility.

In the following, we introduce both models and describe the modifications made to address the previously discussed limitations. The derivation and notation employed for both models closely follow the conventions established in Jazar (2008), specifically regarding tire slip angle α_i , tire heading angle β_i and wheelbase distance l_i with subscript i denoting the front (f) or rear (r) axle (cf. Figure 3 and 4).

2.1 Newton-Euler model

By applying the Newton-Euler equations of motion, one obtains

$$\dot{v}_{x} = F_{x}/m + \omega v_{y}
\dot{v}_{y} = F_{y}/m - \omega v_{x}
\dot{\omega} = M_{z}/I_{z}$$
(2)

where m is the mass, I_z the moment of inertia and F_x , F_y and M_z the expressions for the longitudinal force, lateral force, and yaw moment.

The model accuracy and numerical well-posedness primarily depend on two design aspects: the selection and mathematical formulation of the tire forces, and the implementation of the tire slip angle computation.

We first address the choice of tire forces and derive

$$F_{\rm x} = \sin \delta F_{\alpha,\rm f} + \cos \delta (F_{\rm m} - F_{\rm d})$$

$$F_{\rm y} = \sin \delta (F_{\rm m} - F_{\rm d}) + \cos \delta F_{\alpha,\rm f} + F_{\alpha,\rm r}$$

$$M_{\rm z} = \sin \delta l_{\rm f} (F_{\rm m} - F_{\rm d}) + \cos \delta l_{\rm f} F_{\alpha,\rm f} - l_{\rm r} F_{\alpha,\rm r}$$

$$(3)$$

based on the lateral slip forces $F_{\alpha,i}$ and the longitudinal drag and motor forces $F_{\rm d}$ and $F_{\rm m}$, as illustrated in Figure 3.

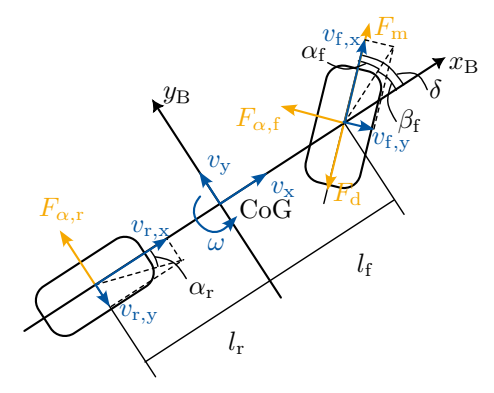


Fig. 3. Newton-Euler bicycle model (velocities in blue, forces in yellow).

While longitudinal tire force is neglected at the rear wheel, we model drag-induced force at the front tire as a second order polynomial

$$F_d = R_1 v_{f,x} + R_2 v_{f,x}^2$$
 (4)

with drag coefficients R_1 and R_2 .

For a bumper car, which generally operates at low speeds and small slip angles, a linear tire force model approximates most of the dynamics, as it captures the proportional relation $F_{\alpha,i} \propto \alpha_i$ in that operating range. Using models with many parameters—such as the Magic Formula—is not practical because those parameters cannot be reliably identified from datasets with limited high-slip tire behavior.

To balance simplicity and realism, a suitable compromise (Zhang and Liu, 2018) is the following piecewise linear tire

$$F_{\alpha,i} = \begin{cases} -C_{\alpha,i} \, \alpha_i & \text{for} \quad |\alpha_i| < \hat{F}_{\alpha,i}/C_{\alpha,i}, \\ -\operatorname{sign}(\alpha_i)\hat{F}_{\alpha,i} & \text{for} \quad |\alpha_i| \ge \hat{F}_{\alpha,i}/C_{\alpha,i} \end{cases}$$
(5)

where $C_{\alpha,i}$ is the cornering stiffness and $\hat{F}_{\alpha,i}$ the maximum lateral tire force of axis $i \in \{f, r\}$, respectively.

The second design aspect of the Newton-Euler model concerns the numerical robustness of tire slip computation, when the velocity vector approaches zero (i.e., the vehicle approaches standstill) and the slip angle α_i loses physical meaning. Kim et al. (2018) introduced an Advanced Slip Ratio (ASR), where a lower bound is imposed on the longitudinal velocity when computing the tire slip angle, thus implying $\alpha \to 0$ for low velocities.

Moreover, the extended steering range induces negative longitudinal velocity, causing the rear wheel to rotate in reverse. As a result, the rear tire slip is given by $\alpha_r = \beta_r - \delta_r$ where δ_r is 0° if the wheel spins forward and 180° if backward. Due to the trigonometric properties of the arctan(·) function, we compute the tire heading angle using the ASR and the absolute value of the longitudinal tire velocity as

$$\alpha_i = \arctan\left(\frac{v_{i,y}}{\max(|v_{i,x}|, v_0)}\right) \tag{6}$$

with longitudinal and lateral tire velocities (cf. Figure 3) defined by

$$v_{\rm f,x} = \cos \delta v_{\rm x} + \sin \delta (v_{\rm y} + l_{\rm f}\omega) \qquad v_{\rm r,x} = v_{\rm x} v_{\rm f,y} = \cos \delta (v_{\rm y} + l_{\rm f}\omega) + \sin \delta v_{\rm x} \qquad v_{\rm r,y} = v_{\rm y} - l_{\rm r}\omega$$
(7)

Kim et al. (2018) shows that the integration of ASR limits the lateral tire dynamics, however, the lateral tire dynamics remain faster than the dynamics of the vehicle body inertia, making the Newton-Euler model stiff. Consequently, discretization ($T=0.1\,\mathrm{s}$) performed using RK4 with two subsequent steps yields the body frame velocity evolution as

$$\mathbf{v}_{k+1} = \begin{bmatrix} v_{x} \ v_{y} \ \omega \end{bmatrix}_{k+1}^{T} = f_{NE}(\mathbf{v}_{k}, \mathbf{u}_{k}). \tag{8}$$

2.2 Kinematic model

By using geometric relations of vehicle chassis in combination with the Instant Center of Rotation (ICR), kinematic models are widely used in path planning. In contrast to typical kinematic models, we derive a formulation with two major adaptations regarding the system representation and assumptions on the tire slip.

First, conventional kinematic models typically represent the system state using the velocity at the Center of Gravity (CoG) (Jazar, 2008; Ghosn et al., 2024). While this choice is appropriate for vehicles exhibiting minimal tire deflection, it proves suboptimal for the bumper car, where the CoG velocity exhibits a significant correlation with the steering angle. Owing to the presence of a motorized front wheel, the front-wheel velocity $v_{\rm f}$ emerges as a directly actuated and thus more suitable state variable for system representation in this context.

Secondly, the assumption of slip-free movement does not hold in our context. Therefore, we derive the kinematic formulation considering the tire slip, similar to Ghosn et al. (2024). The kinematic bicycle model is depicted in Figure 4 with the corresponding set of equations

$$v_{x} = \cos \beta_{f} v_{f}$$

$$v_{y} = \frac{l_{f} \sin \beta_{f} + l_{r} \cos \beta_{f} \tan \beta_{r}}{l_{f} + l_{r}} v_{f}$$

$$\omega = \frac{\sin \beta_{f} - \cos \beta_{f} \tan \beta_{r}}{l_{f} + l_{r}} v_{f}$$
where $\beta_{f} = \delta + \alpha_{f}$, $\beta_{r} = \alpha_{r}$. (9)

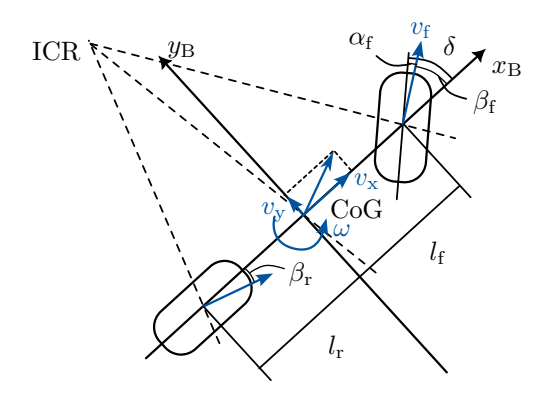


Fig. 4. Kinematic bicycle model (velocities in blue). which describe the static output function

$$\boldsymbol{v}_k = g_{\rm kin}(\boldsymbol{x}_k)$$
 with $\boldsymbol{x}_k = \left[v_{\rm f} \ \alpha_{\rm f} \ \alpha_{\rm r} \ \delta\right]^T$. (10) The evolution of δ follows from the time discretization of (1). The dynamics of the remaining state $\left[v_{\rm f} \ \alpha_{\rm f} \ \alpha_{\rm r}\right]^T$ are not explicitly characterized from first principles. Rather, they are assumed to follow the general discrete-time model representation:

$$\tilde{\boldsymbol{x}}_{k+1} = \left[v_{\mathrm{f}} \ \alpha_{\mathrm{f}} \ \alpha_{\mathrm{r}}\right]_{k+1}^{T} = f_{\mathrm{kin}}(\boldsymbol{x}_{k}, \boldsymbol{u}_{k}), \tag{11}$$

where $f_{\rm kin}$ denotes a kinematic evolution function. This function is subsequently obtained via data-driven system identification, as detailed in Section 3, incorporating physical insights based on motor actuation and slip dynamics.

3. DATA-DRIVEN MODELING

Despite the modifications introduced in the previous section, the models continue to exhibit inherent limitations, notably the challenge of accurately obtaining all necessary parameters through direct measurement as well as the computational requirements associated with numerical stiffness. To overcome these limitations, data-driven methods are increasingly utilized for vehicle modeling because they can learn complex behaviors directly from data, offering faster inference and adaptability to unmodelled dynamics.

Firstly, we discuss identification of the white-box models via data-driven optimization.

Secondly, black-box approaches using multilayer perceptrons (MLPs) are investigated. We will show that these models are capable of capturing complex nonlinearities but suffer from limited physical interpretability and sensitivity to data quality, which complicates reliable online adaptation. Technical details for the implementation are reported in Appendix C.

Eventually, grey-box methods are employed to merge the advantages of both approaches. By incorporating physical knowledge within a kinematic bicycle framework through Sparse Identification of Nonlinear Dynamical Systems (SINDy), an explicit and interpretable model structure is obtained. Finally, we propose a hybrid residual modeling approach that combines the strengths of physics-based models and neural networks, enhancing prediction accuracy while preserving interpretability.

In all modeling approaches the training objective involves minimizing the Normalized Mean Squared Error (NMSE) $\,$

$$L(\hat{\boldsymbol{q}}, \boldsymbol{q}) = \frac{1}{nN} \sum_{k=1}^{N} \| \boldsymbol{W} (\hat{\boldsymbol{q}}_k - \boldsymbol{q}_k) \|_2^2$$
 (12)

with generic predicted sequence $\hat{q} = \left\{\hat{q_k}\right\}_{k=1}^N$, $\hat{q_k} \in \mathbb{R}^n$, measured sequence $q = \left\{q_k\right\}_{k=1}^N$, $q_k \in \mathbb{R}^n$ and diagonal normalization matrix $\boldsymbol{W} \in \mathbb{R}^{n \times n}$ to ensure consistent and comparable evaluation of prediction accuracy across models. The two sequences will be specified when discussing the individual identification methods.

3.1 White-box modeling

The geometric parameters of the Newton–Euler model $(l_{\rm f}, l_{\rm r}, m, \hat{\delta})$ and parameters related to the actuators $(d, T_{\rm s})$ can be directly measured or obtained from hardware specifications. However, a subset of model parameters are unknown or difficult to measure accurately. Therefore, they are estimated with a genetic algorithm due to the highly nonlinear and partially non-differentiable dependence of the model outputs on its parameters (Goldberg, 1991). The training is performed by minimizing the NMSE on the one-step body frame velocity predictions, namely setting $\hat{q} = f_{\rm NE}(v, u)$ and q = v in (12). The resulting parameters are reported in Appendix B.

3.2 Black-box modeling

The first model we consider is a Nonlinear AutoRegressive model with eXogenous inputs implemented as an MLP (NARX-MLP) to capture actuators and vehicle dynamics while remaining independent of previous kinematic assumptions. In particular, the velocity evolution is described by

 $\mathbf{v}_{k+1} = f_{\text{NARX-MLP}}(\mathbf{v}_k, \dots, \mathbf{v}_{k-n_y}, \mathbf{u}_k, \dots, \mathbf{u}_{k-n_u})$ (13) with $n_y = n_u = 2$. The training is performed by minimizing the NMSE on the one-step body frame velocity predictions, namely setting $\hat{\mathbf{q}} = f_{\text{NARX-MLP}}(\mathbf{v}, \mathbf{u})$ and $\mathbf{q} = \mathbf{v}$ in (12).

For the second model, we approximate the kinematic state transition (11) with a multilayer perceptron (K-MLP):

$$\tilde{\boldsymbol{x}}_{k+1} = f_{K-MLP}(\boldsymbol{x}_k, \boldsymbol{u}_k) \tag{14}$$

The training is performed minimizing the NMSE on the one-step state predictions, namely setting $\hat{q} = f_{\text{K-MLP}}(\boldsymbol{x}, \boldsymbol{u})$ and $q = \tilde{\boldsymbol{x}}$ in (12).

While these models lack physical interpretability, they provide a baseline for comparison against grey-box models, where physical knowledge of the system is explicitly incorporated to improve interpretability and potentially enhance prediction robustness.

3.3 Grey-box modeling

The SINDy algorithm infers governing equations from data by representing the kinematic state transition (11) as a sparse linear combination of candidate nonlinear functions

$$f_{\text{SINDy}}(\boldsymbol{x}_k, \boldsymbol{u}_k) = \boldsymbol{\Xi} \boldsymbol{\Theta}^T(\boldsymbol{x}_k, \boldsymbol{u}_k).$$
 (15)

The function library $\mathbf{\Theta}^T(\mathbf{x}_k, \mathbf{u}_k)$ is constructed based on available physical insight: generic polynomial terms are

used when prior knowledge is limited, whereas trigonometric or physically motivated functions can be included to capture expected behaviors such as periodicity or symmetry. The coefficient vector Ξ contains the weights assigned to each candidate function, and sparsity constraints are applied to identify only the few terms that significantly contribute to the system dynamics (de Silva et al., 2020; Kaptanoglu et al., 2022). The candidate libraries Θ_i consisting of entries $q_{i,j}$ are derived as follows.

The front-wheel velocity is primarily affected by the motor throttle and braking, the rolling resistance, and the drag induced by tire slip. The throttle is the only energy-supplying input, active when the motor input $u_{\rm m}$ exceeds the measured velocity $v_{\rm f}$. Following the proportional feedback behavior of the motor controller, the candidate terms

$$q_{v,1} = \max(0, u_m - v_f), \qquad q_{v,2} = \max(0, u_m - v_f) v_f$$
(16)

are included. Braking effects are modeled as dissipative and proportional to negative brake input $u_{\rm m} \leq 0$, using

$$q_{\rm v,3} = {\rm min}(0,u_{\rm m})v_{\rm f}, \qquad q_{\rm v,4} = {\rm min}(0,u_{\rm m})v_{\rm f}^2.$$
 (17)
Rolling resistance is represented by a third order polynomial in $v_{\rm f}$ and included with the terms

$$q_{v,5} = v_f, \quad q_{v,6} = v_f^2, \quad q_{v,7} = v_f^3.$$
 (18)

Additional resistance due to tire slip is modeled through polynomial combinations of $v_{\rm f}$, $|\alpha_{\rm f}|$, and steering quantities $|\delta|$ and $|\dot{\delta}|$. Instances of such candidate terms are

$$q_{\text{v},9} = v_{\text{f}} |\alpha_{\text{f}}|, \quad q_{\text{v},12} = v_{\text{f}} |\dot{\delta}|, \quad q_{\text{v},16} = v_{\text{f}} |\dot{\delta}| |\alpha_{\text{f}}|.$$
 (19)
Terms independent of v_{f} are excluded to ensure dissipative behavior, i.e., $\dot{v}_{\text{f}} \to 0$ as $v_{\text{f}} \to 0$.

The slip-angle dynamics originate from the balance between the lateral tire forces and the vehicle motion. Because slip angles vanish at standstill, each candidate term contains $v_{\rm f}$ except the slip angle itself. The antisymmetric relation between turn and slip direction is enforced via absolute-value operators. This leads to the introduction of the terms

$$q_{\alpha,1} = \alpha_{\rm f}, \quad q_{\alpha,2} = v_{\rm f}\delta, \quad q_{\alpha,5} = v_{\rm f}\dot{\delta}, \quad q_{\alpha,8} = v_{\rm f}\delta|\dot{\delta}|.$$
 (20)

The model obtained via SINDy regression (K-SINDy)

$$\tilde{\boldsymbol{x}}_{k+1} = f_{\text{SINDv}}(\boldsymbol{x}_k, \boldsymbol{u}_k) \tag{21}$$

leverages the physics-informed library described above to produce interpretable representations. The resulting state equation is reported in Appendix D.

With SINDy being inherently limited to the terms defined in the candidate library, its accuracy is limited in comparison to universal function approximators such as neural networks. To bridge this gap, we propose a K-SINDy-MLP model where the K-SINDy state transition equation is augmented by a MLP

$$\tilde{\boldsymbol{x}}_{k+1} = f_{\text{SINDy}}(\boldsymbol{x}_k, \boldsymbol{u}_k) + f_{\text{RES-MLP}}(\boldsymbol{x}_k, \boldsymbol{u}_k)$$
. (22) The training is performed on the NMSE of the one-step state prediction residual error $\boldsymbol{e}_{k+1} = \tilde{\boldsymbol{x}}_{k+1} - f_{\text{SINDy}}(\boldsymbol{x}_k, \boldsymbol{u}_k)$, namely setting $\hat{\boldsymbol{q}} = f_{\text{RES-MLP}}(\boldsymbol{x}_k, \boldsymbol{u}_k)$ and $\boldsymbol{q} = \boldsymbol{e}$ in (12).

Since the residual network only learns corrections to a meaningful analytic model, it requires fewer neurons and training iterations compared to the K-MLP model (14). This approach thus combines interpretability and faster execution with the accuracy of neural network approximation.

4. EXPERIMENTAL VALIDATION

All data were recorded in a rectangular bumper-car arena of approximately $7 \times 12\,\mathrm{m}$. The bumper car pose p was measured by an OptiTrack motion-capture system using eight cameras placed around the perimeter. The body–fixed velocities v or kinematic state x according to (10) are not directly measured and are therefore estimated with an Extended Kalman Filter (EKF) described in Appendix A. We recorded slightly over one hour of driving at 10 Hz, covering a wide range of operating scenarios. The dataset was then split into validation data (110 s) and training data (the remaining part).

The comparison metrics associated with the models presented in Section 3 are reported in Table 1. We evaluate each model by initializing it with the starting sample of the validation dataset and driving it with the validation input sequence. By comparing the resulting predicted trajectory against the actual validation trajectory, we assess performance in terms of the NMSE and the total computational time required for the simulation.

Table 1. Comparison of derived models.

${\rm NMSE} \times 10^3$	Computation time in ms
5.973	303.7
5.587	76.2
4.594	85.6
12.960	37.1
4.765	81.1
	5.973 5.587 4.594 12.960

The comparative analysis of all modeling approaches highlights the distinct strengths and trade-offs associated with interpretability, computational efficiency, and predictive accuracy. The Newton-Euler model provides full physical interpretability but is limited by computational stiffness, resulting in slower simulation $(3.6-8.2 \times \text{slower than the})$ K-MLP and K-SINDy) and only modest accuracy. On the other hand, purely black-box models such as NARX-MLP and K-MLP trade interpretability for higher expressiveness. Moreover, K-MLP achieves the highest prediction accuracy with moderate computation time. The K-SINDy approach, constructed from a physically motivated function library, achieves the fastest prediction time due to its analytically sparse structure and offers a degree of interpretability, but its accuracy is lower than the other models due to its limited function library. The hybrid K-SINDy-MLP model effectively balances these competing objectives: by integrating physical knowledge (kinematic constraints and physically motivated SINDy) with the expressiveness of data-driven residual corrections (via MLP), it maintains medium interpretability, achieves computation times suitable for real-time application while remaining comparable in accuracy to K-MLP. Additional considerations on models comparison are reported in Appendix E.

To conclude this analysis, we compare the Newton–Euler and the K-SINDy-MLP models to highlight the improvements obtained through data-driven modeling. Figure 5 and Figure 6 illustrate a validation trajectory extracted

from the dataset and the corresponding predicted trajectories obtained with the two models. At several points along the trajectories, marked by crosses, the predicted state is reinitialized to the true validation state to test different initial conditions. A close-up view between 66.4 and 68.4 seconds captures the vehicle's transition from backward motion (steering angle exceeding 90°) to forward motion (steering angle below 90°). Within this critical segment, it is evident that the K-SINDy-MLP model substantially outperforms the Newton–Euler model (as well as its linearized version, see Figure 2) in accurately predicting the vehicle's state, highlighting the superior capacity of the hybrid approach to manage complex dynamical regimes.

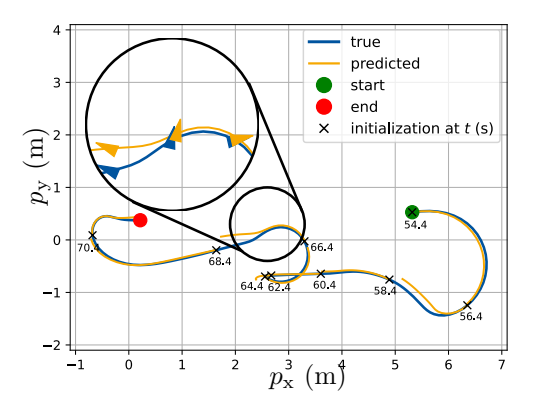


Fig. 5. Comparison between the experimental vehicle trajectory and the predicted trajectory obtained with the Newton-Euler model. The model is reinitialized every two seconds to test its effectiveness in different scenarios.

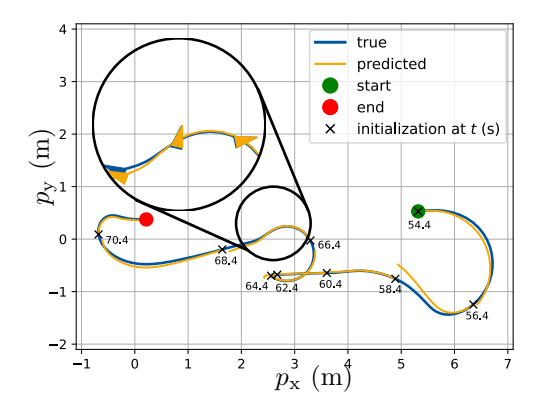


Fig. 6. Comparison between the experimental vehicle trajectory and the predicted trajectory obtained with the K-SINDy-MLP model. The model is reinitialized every two seconds to test its effectiveness in different scenarios.

5. CONCLUSION

This paper investigates several modeling approaches for highly maneuverable autonomous bumper cars, comparing physical, data-driven, and hybrid frameworks. The Newton-Euler model is physically accurate but is computationally expensive. MLP models offer high accuracy and moderate runtime but lack physical interpretability, while SINDy kinematic models run fastest but with lower accuracy. Combining physical insights with neural network

corrections (K-SINDy-MLP) provides a balance of speed, accuracy, and interpretability, making it well suited for real-time collision avoidance and control tasks in challenging scenarios.

Future research will concern a more refined distribution of effects in hybrid modeling. For instance, one could exclude deceleration terms from the base model and enforce dissipativity in the velocity residual MLP (Okamoto and Kojima, 2024) to ensure that the correction only models additional drag rather than artificial energy injection.

ACKNOWLEDGEMENTS

The authors would like to thank Yannick Soller for his technical assistance with the experimental setup. His support in collecting data on the real system is gratefully acknowledged.

REFERENCES

- Chen, J., Yu, C., and Wang, Y. (2024). Hybrid modeling for vehicle lateral dynamics via agru with a dual-attention mechanism under limited data. *Control Engineering Practice*, 151, 106015.
- Chrosniak, J., Ning, J., and Behl, M. (2024). Deep dynamics: Vehicle dynamics modeling with a physics-constrained neural network for autonomous racing. *IEEE Robotics and Automation Letters*, 9(6), 5292–5297.
- de Silva, B., Champion, K., and Quade, M. (2020). Pysindy: A python package for the sparse identification of nonlinear dynamical systems from data. *Journal of Open Source Software*, 5(49), 2104.
- Frogerais, P., Bellanger, J.J., and Senhadji, L. (2012). Various ways to compute the continuous-discrete extended kalman filter. *IEEE Transactions on Automatic Control*, 57(4), 1000–1004.
- Ghosn, A.B., Polack, P., and de La Fortelle, A. (2024). The hybrid extended bicycle: A simple model for high dynamic vehicle trajectory planning.
- Goldberg, D.E. (1991). Genetic algorithms as a computational theory of conceptual design. Applications of Artificial Intelligence in Engineering VI.
- Jain, A., O'Kelly, M., and Chaudhari, P. (2020). Bayesrace: Learning to race autonomously using prior experience.
- Jazar, R.N. (2008). Vehicle dynamics Theory and Application, volume 1. Springer.
- Kaptanoglu, A.A., de Silva, B.M., and Fasel, U. (2022). Pysindy: A comprehensive python package for robust sparse system identification. *Journal of Open Source Software*, 7(69), 3994.
- Kim, T.Y., Jung, S., and Yoo, W.S. (2018). Advanced slip ratio for ensuring numerical stability of low-speed driving simulation: Part ii—lateral slip ratio. *Proceedings of the Institution of Mechanical Engineers, Part D: Journal of Automobile Engineering*, 233, 095440701880704. doi:10.1177/0954407018807040.
- Kim, T., Lee, H., and Lee, W. (2022). Physics embedded neural network vehicle model and applications in riskaware autonomous driving using latent features.
- Kong, J., Pfeiffer, M., and Schildbach, G. (2015). Kinematic and dynamic vehicle models for autonomous driv-

- ing control design. In 2015 IEEE Intelligent Vehicles Symposium (IV), 1094–1099.
- Lillo, L.D., Gode, T., and Zhou, X. (2023). Comparative safety performance of autonomous- and human drivers: A real-world case study of the waymo one service.
- Okamoto, Y. and Kojima, R. (2024). Learning deep dissipative dynamics.
- Pacejka, H. (2005). Tire and vehicle dynamics. Elsevier.
 Paparazzo, F., Castoldi, A., and Sathyamangalam Imran,
 M.I.I. (2025). Learning-based mpc leveraging sindy for vehicle dynamics estimation. Electronics, 14(10).
- Parczewski, K. and Romaniszyn, K.M. (2017). Modelling of the influence of tire characteristics on stability of motion with using vehicle at a scale. *Journal of KONES*, 24.
- Rhode, S., Jarmolowitz, F., and Berkel, F. (2024). Vehicle single track modeling using physics guided neural differential equations.
- Saglam, F. and Unlusoy, Y.S. (2011). Identification of low order vehicle handling models from multibody vehicle dynamics models. In 2011 IEEE International Conference on Mechatronics, 96–101.
- Zhang, Q. and Liu, Z. (2018). A novel piecewise affine model for vehicle lateral dynamics. *IEEE Access*, 6, 78493–78502. doi:10.1109/ACCESS.2018.2885050.

Appendix A. STATE ESTIMATION

While the OptiTrack system provides the rigid-body pose \boldsymbol{p} of the vehicle, the body–fixed velocities \boldsymbol{v} are not directly measured and are therefore estimated with an Extended Kalman filter (EKF). The continuous-time state is

$$\boldsymbol{x}_{\mathrm{KF}} = [p_{\mathrm{x}} \ p_{\mathrm{y}} \ \theta \ v_{\mathrm{f}} \ \beta_{\mathrm{f}} \ \beta_{\mathrm{r}} \ \delta]^{T}$$
 (A.1)

where the first three states correspond to the measurement vector. The bumper car model with process noise $\mathbf{w} = [w_{\text{v}} \ w_{\beta \text{f}} \ w_{\beta \text{r}}]^T$ is

$$\dot{\boldsymbol{x}}_{\mathrm{KF}} = f(\boldsymbol{x}_{\mathrm{KF}}, \boldsymbol{w}) = \begin{bmatrix} \cos\theta \, v_{\mathrm{x}} + \cos\theta \, v_{\mathrm{y}} \\ \sin\theta \, v_{\mathrm{x}} - \sin\theta \, v_{\mathrm{y}} \\ \omega \\ w_{\mathrm{v}} \\ \eta \, (1 - \gamma)(\delta - \beta_{\mathrm{f}}) + w_{\beta \mathrm{f}} \\ \eta \, (1 - \gamma)(-\beta_{\mathrm{r}}) + w_{\beta \mathrm{r}} \\ \mathrm{sat}_{[-d, d]}((u_{\mathrm{s}} - \delta)/T_{\mathrm{s}}) \end{bmatrix}$$
(A.2)

with $\gamma=(\tanh(10\,v_{\rm f}-1)+1)/2$ and $\eta=20$. The body velocities $v_{\rm x},v_{\rm y},\omega$ are calculated using the kinematic model (9). The term γ drives the slip angles to zero as $v_{\rm f}\to 0$ to avoid drift when they become unobservable; η sets the associated pole. State and covariance are propagated using Runge-Kutta 4 (RK4) discretizations, following Frogerais et al. (2012).

Appendix B. GENETIC ALGORITHM FOR PARAMETER OPTIMIZATION OF THE NEWTON-EULER MODEL

A genetic algorithm is employed for parameter identification of the Newton-Euler model due to the highly nonlinear and partially non-differentiable dependence of the model outputs on its parameters. The algorithm is implemented using MATLAB ga() function of the Global

Optimization Toolbox with a population of 150 individuals and default hyperparameters. Reasonable parameter ranges are assessed prior to optimization (for cornering stiffness C_{α} cf. Saglam and Unlusoy (2011); Parczewski and Romaniszyn (2017)) and accounted for in population initialization.

The parameters of the Newton-Euler model after optimization are given in Table B.1.

Table B.1. Parameters of the derived Newton-Euler vehicle model. Parameters are either derived from measurements, or GA-optimization (the latter is indexed by *).

Name	Variable	Value	Unit
Steering			
Maximum steering angle	$\hat{\delta}$	2.012	rad
Maximum stepper speed	d	1.418	rad/sec
Stepper motor time constant	$T_{ m s}$	0.155	S
Motor			
Maximum motor force*	$\hat{F}_{\mathbf{m}}$	423.4	N
Throttle proportional gain*	$K_{ m t}$	274.8	Nsec/m
Throttle reference velocity*	c	2.033	m/s
Brake proportional gain*	$K_{ m b}$	597.0	Ns/m
Car Body			
Mass of vehicle and driver	m	319.6	kg
Moment of inertia*	$I_{ m z}$	90.85	$kg \cdot m^2$
Wheelbase front	$l_{ m f}$	0.54	m
Wheelbase rear	$l_{ m r}$	0.33	m
Tire			
Cornering stiffness front*	$C_{\alpha,f}$	3594.0	N/rad
Cornering stiffness rear*	$C_{lpha,\mathrm{r}}$	7840.0	N/rad
maximum front tire force*	$\hat{F}_{lpha,\mathrm{f}}$	629.6	N/rad
maximum rear tire force*	$\hat{F}_{lpha,\mathrm{r}}$	1360.0	N/rad
Linear front wheel drag*	R_1	43.40	Ns/m
Quadratic front wheel drag*	R_2	-15.61	$N(s/m)^2$

Appendix C. HYPERPARAMETERS OF MLP-TRAINING

All models are implemented in PyTorch and trained to minimize the mean squared one-step prediction error. A feedforward MLP with two hidden layers of 256 and 128 neurons and ReLU activation functions is used for NARX-MLP and K-MLP, and halved number of neurons for K-SINDy-MLP. Training uses the Adam optimizer with a batch size of 256, weight decay $\lambda=10^{-5}$, and an initial learning rate of $5\cdot 10^{-5}$, which is reduced by a factor of 0.6 every 40 epochs. Dropout regularization is active during training but disabled in validation. All inputs to the neural network are normalized. Each epoch consists of one gradient descent step per batch, ensuring balanced sample contribution.

Appendix D. SINDY REGRESSION AND MODEL PARAMETERS

We use the SINDy framework implemented in PySINDy (de Silva et al., 2020; Kaptanoglu et al., 2022). All states entering the candidate matrices are scaled accordingly to ensure consistent thresholding.

From SINDy regression we derive the following state equations:

$$\begin{split} v_{\mathrm{f},k+1} &= (0.968v_{\mathrm{f}} + 0.0379v_{\mathrm{f}}^2 - 0.0155v_{\mathrm{f}}^3 - 0.475\alpha_{\mathrm{f}}^2 \\ &\quad + 0.053\max(u_{\mathrm{m}}c - v_{\mathrm{f}}, 0)(1 + 0.487v_{\mathrm{f}}) \\ &\quad + 0.181\min(u_{\mathrm{m}}v_{\mathrm{f}}, 0)(1 - 0.462v_{\mathrm{f}}))_k \quad \text{(D.1a)} \end{split}$$

$$\alpha_{\mathrm{f},k+1} &= (0.777\alpha_{\mathrm{f}} + 0.00718v_{\mathrm{f}}\delta|\delta| - 0.0117v_{\mathrm{f}}^2\delta \\ &\quad + 0.0259v_{\mathrm{f}}\dot{\delta} - 0.0169v_{\mathrm{f}}\dot{\delta}|\dot{\delta}| - 0.0169v_{\mathrm{f}}^2\dot{\delta} \\ &\quad - 0.00836v_{\mathrm{f}}\dot{\delta}\delta^2)_k \quad \text{(D.1b)} \end{split}$$

$$\alpha_{\mathrm{r},k+1} &= (-0.0485\alpha_{\mathrm{f}} + 0.0147v_{\mathrm{f}}\delta - 0.0127v_{\mathrm{f}}\delta|\delta| \\ &\quad - 0.00661v_{\mathrm{f}}\dot{\delta}|\delta| + 0.00580v_{\mathrm{f}}\dot{\delta}\delta^2)_k \quad \text{(D.1c)} \end{split}$$

Appendix E. DISCUSSION ON PREDICTIVE ACCURACY

We compare the state prediction of the K-SINDy and K-SINDy-MLP in Figure E.1. A clear improvement in state prediction can be seen compared to the sparse kinematic model. While performance of both models is quite accurate in the first 50s, K-SINDy-MLP excels in regimes with high-dynamic turns and rapid steering. Most prominently, slip induced deceleration at $t\approx 65$ s, $t\approx 78$ s and $t\approx 97$ s is underestimated by K-SINDy.

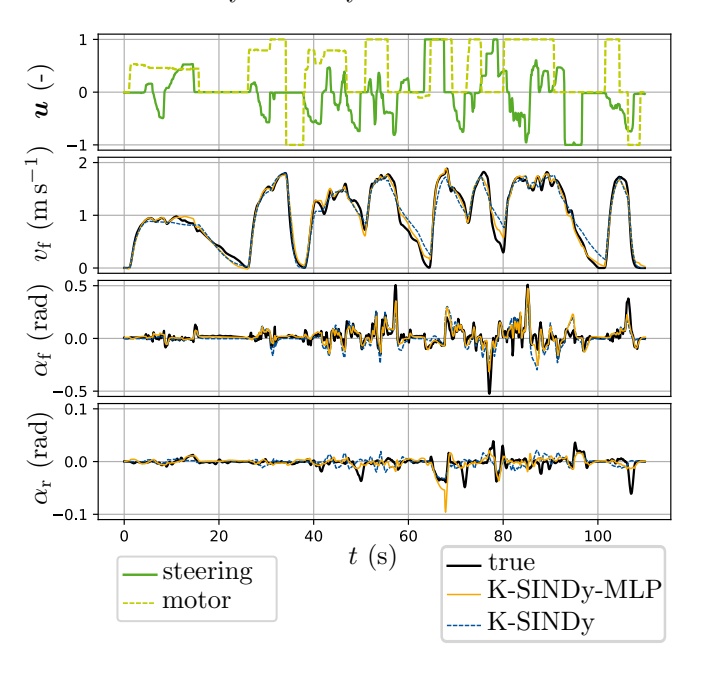


Fig. E.1. Closed-loop state predictions of the validation sequence of the derived K-SINDy and K-SINDy-MLP models.

For the same sequence, the NARX-MLP achieves comparable fidelity but exhibits its largest deviation during backward motion at high steering at $t \approx 66 \,\mathrm{s}$. A possible explanation can be found in the lack of kinematic constraints and internal steering dynamics. The Newton-Euler model reproduces motor impact and sliding effects closely; small under-deceleration occurs at low $v_{\rm f}$.